

Deep-Learning Enabled Active Biomimetic Multifunctional Hydrogel Electronic Skin

Kai Tao, Jiahao Yu, Jiyuan Zhang, Aocheng Bao, Haowen Hu, Tao Ye, Qiongling Ding, Yaozheng Wang, Haobin Lin, Jin Wu,* Honglong Chang, Haixia Zhang,* and Weizheng Yuan*



Cite This: *ACS Nano* 2023, 17, 16160–16173



Read Online

ACCESS |

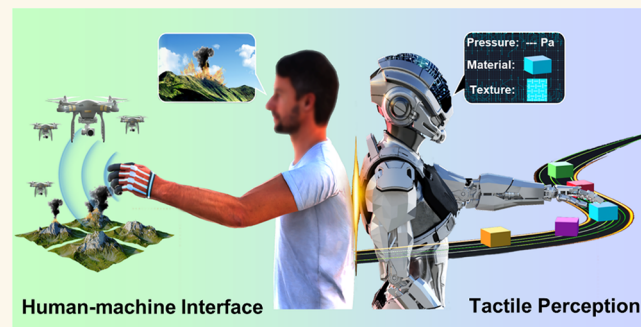
Metrics & More

Article Recommendations

Supporting Information

ABSTRACT: There is huge demand for recreating human skin with the functions of epidermis and dermis for interactions with the physical world. Herein, a biomimetic, ultrasensitive, and multifunctional hydrogel-based electronic skin (BHES) was proposed. Its epidermis function was mimicked using poly(ethylene terephthalate) with nanoscale wrinkles, enabling accurate identification of materials through the capabilities to gain/lose electrons during contact electrification. Internal mechanoreceptor was mimicked by interdigital silver electrodes with stick-slip sensing capabilities to identify textures/roughness. The dermis function was mimicked by patterned microcone hydrogel, achieving pressure sensors with high sensitivity (17.32 mV/Pa), large pressure range (20–5000 Pa), low detection limit, and fast response (10 ms)/recovery time (17 ms). Assisted by deep learning, this BHES achieved high accuracy and minimized interference in identifying materials (95.00% for 10 materials) and textures (97.20% for four roughness cases). By integrating signal acquisition/processing circuits, a wearable drone control system was demonstrated with three-degree-of-freedom movement and enormous potentials for soft robots, self-powered human–machine interaction interfaces of digital twins.

KEYWORDS: E-Skin, Triboelectric nanogenerator, Human machine interface, Hydrogel, Deep learning



1. INTRODUCTION

Human skin is extremely crucial for its protective, immunological, and tactile functions. Inspired by the natural human skin, scientists have developed various types of electronic skins (e-skins).^{1,2} The tactile sensing capability is critical for these electronic skins; for example, it allows intelligent robots to interact effectively with their environment.^{3,4} A variety of pressure sensing techniques have been developed for e-skins based on various mechanisms such as piezoresistive,^{5,6} capacitive,^{7,8} piezoelectric,^{9,10} and triboelectric ones.^{11,12} In addition to pressure sensing, identification/recognition of different types of material or texture/roughness is also essential for the e-skin, especially when the robots are required to have real intelligence to interact with their surroundings.^{13–15} However, so far, a comprehensive e-skin, which can simultaneously detect the pressure, material/substance, and texture/roughness, has rarely been reported.

The structural layers of human skin include the epidermis, dermis, and hypodermis. To mimic this multilayer skin structure, researchers have proposed several types of e-skins with similar functions and properties as the human skin.^{16–20} The dermis, one of the three main components of human skin, is responsible for keeping the skin supple and elastic and also

acting as a fluid reservoir. It also protects the blood capillaries, glands, and other substances in the skin tissue.^{21,22} Additionally, it generates ion channels in this region, providing absorption channels for moisture and nutrients.^{23–25} The tactile sense functions of the natural skin were proven to be mostly due to existence of mechanoreceptors within the dermis.²⁶ Previous e-skin-related studies have been mostly concentrated more on achieving the function of pressure detection, whereas the other functions of the dermis have seldom been achieved in electronic skin.^{27–30}

Recently, hydrogels have received widespread interest because their mechanical structures and physical properties are similar to those of human tissue, and they have notable benefits of ultrahigh flexibility, exceptional stretchability, transparency in the visible spectrum, tunable conductivity,

Received: June 11, 2023

Accepted: July 27, 2023

Published: July 31, 2023



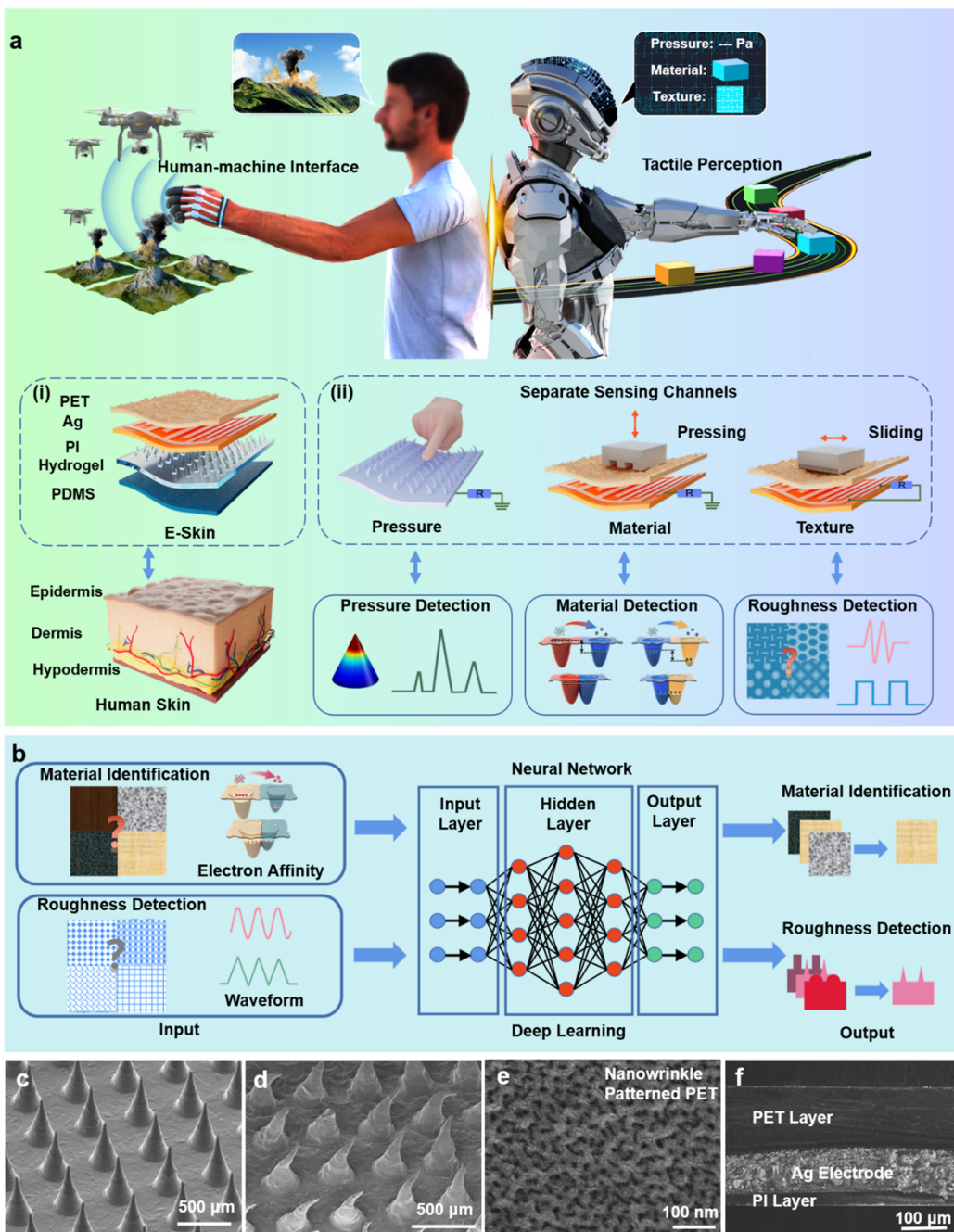


Figure 1. Structure design of the BHES. (a) Schematic illustration depicting the detailed structure (i), sensing mode (ii), and application scenarios of BHES as a human–machine interaction interface. (b) Flowchart of AI-assisted precise material and roughness detection via stick-slip and contact electrification. (c) SEM image of the microcone patterned hydrogel. (d) SEM image of deformed microcone patterned hydrogel under pressure. (e) SEM image of the nano wrinkled structure of PET surface. (f) Cross-sectional SEM image of the PET–Ag–PI multilayered structure.

and intrinsic biocompatibility.^{31–35} Hydrogels have been utilized in multiple kinds of sensors (temperature, humidity, strain, gases, etc.) and triboelectric nanogenerators for human–machine interfaces (HMIs).^{36–39} The ions inside the ionic conductive hydrogels endow them with good conductivity.^{40–42} The porous structure of the hydrogel provides effective channels for the conduction of ions. Also, the networks formed inside the hydrogels offer superior mechanical and functional properties, such as deformability, elasticity, etc., notably in the double-network (DN) hydrogels. However, the abundant water in the hydrogels is an obstacle for practical

applications. The water would be evaporated at high temperatures or even at room temperature, resulting in drastic changes in their conductivity and flexibility.^{43,44} On the other hand, hydrogels are prone to becoming frozen and brittle at low temperatures, which limits their future employment in harsh environments.^{45–47} Developing the hydrogels with anti-dehydration and antifreezing capacities is urgently demanded to overcome the bottleneck of their applications.

For recognition/identification of different types of materials, the triboelectric effect and stick–slip mechanisms have been applied.^{48–50} To generate the triboelectric effect, a single-

electrode triboelectric nanogenerator (SE-TENG) was often chosen due to the multiple available contacting materials, while another contacting material was fixed when the SE-TENG was constructed.^{51,52} Due to the different electron affinity of materials, the output peak voltages are different when the SE-TENG comes into contact with various types of materials.⁵³ However, experimental results showed that the contact normal pressure has also a significant effect on the output voltage of SE-TENG.^{54–57} Therefore, influences of two key factors (i.e., pressure and the types of contacting materials) could not be easily separated or identified from the single output voltage signals of SE-TENG. This has caused severe problems for achieving multiple functions of material recognition and pressure detection. For generating the stick-slip phenomenon, the texture/roughness of materials will create diverse vibration signals when the sensor is sliding on the surface of an object, which can be applied as the key mechanism for identification/recognition of texture/roughness of materials.^{58–60} Nevertheless, when different types of materials have a similar or even nearly identical surface feature, texture, or roughness, distinguishing them using this stick-slip phenomenon becomes very challenging.

To solve these critical issues, herein, a biomimetic, ultrasensitive, and multifunctional hydrogel-based electronic skin (BHES), integrating nanoscale wrinkled poly(ethylene terephthalate) (PET) and microcone patterned DN hydrogels was proposed, as shown in Figure 1a. Based on the principle of single-electrode contact-separation and freestanding triboelectric-layer mode TENG, the BHES could disentangle the pressure stimulus and the contacting material electron affinity due to the elaborately built multilayer structure and independent sensing channels.

- In the previous studies,^{61,62} the pressure detection and material type recognition via triboelectric effect were mostly dependent on the recording of maximum output voltage of the TENGs, which often caused the entangled signals of pressure or materials types. In this study, an electronic skin with a specially designed structure and multifunctionality is proposed with minimized mutual interference.
- An antifreezing and antidrying DN hydrogel was developed in this study to better mimic the structure and functionality of the dermis. The advantages of using the proposed microcone structure over the conventional micropyramid structure and microprism structure have been verified using theoretical analysis and finite element simulations. This microcone structure on the surface of the hydrogel was produced using micro-electromechanical systems (MEMS)-enabled technologies. In comparison to the prior work,¹¹ this microcone structure has a much higher shape-filling degree, thus achieving a lower minimum detection limit for the pressure sensor.
- The BHES has high sensitivity and low detection limit when it is served as a pressure sensor, allowing it to detect pressures as low as 20 Pa, such as the fall of a rose petal or a cicada wing. Furthermore, with the aid of deep learning, the identification accuracy for 10 types of material recognition and 4 types of surface roughness has reached up to 95.00% and 97.20%, respectively, demonstrating excellent application prospects in the field of soft robots. By integrating the signal acquisition and wireless signal transmission circuit with the proposed

BHES, convenient human-machine interaction (drone controlled) technique is developed. By converting subtle finger movement into electrical signals, the BHES could aid in the direct control of drone and also the drone swarms. This work could be developed for the critical applications such as monitoring of forest fires in environmental protection and convenient unmanned aerial vehicle (UAV) control in an antiterrorism scenario.

2. RESULTS AND DISCUSSION

2.1. Design of Biomimetic Artificial Skin. In this work, a biomimetic, ultrasensitive, and multifunctional hydrogel-based electronic skin was proposed, and the nanoscale wrinkle patterned PET and microcone patterned DN hydrogel was introduced to the BHES. This BHES can continuously convert the tiny mechanical stimuli into electrical signals. As shown in Figure 1a(i), the proposed e-skin is primarily composed of multilayered structures, i.e., a top layer of nanoscale wrinkle patterned PET, an interdigital silver electrode sandwiched between PET and polyimide (PI), anti-dehydration and antifreezing microcone patterned DN hydrogel electrode, and polydimethylsiloxane (PDMS) substrate. The epidermis is mimicked by using nanoscale wrinkle patterned PET, which enables accurate identification of material type according to different capabilities of various materials to gain or lose electrons during contact electrification. The inside mechanoreceptor is mimicked using an interdigital silver electrode to identify the material texture based on a stick-slip sensing mechanism. Also, as the counterpart of dermis, hydrogel renders the fabricated e-skin supple and elastic, and it could also serve as a fluid reservoir and buffer. Because of the multilayer construction of the BHES, the simplicity of the device is preserved. The device is around 20 mm × 20 mm in size and has an overall thickness about 1 mm. The detailed resemblance between the proposed highly bionic e-skin and human skin is summarized in Table S1, Supporting Information. Figure 1a(ii) depicts the basic operation modes of the BHES, which could detect the modest normal pressure without an external power supply based on the coupling of the triboelectric effect and electrostatic induction by using the microcone patterned hydrogel. In addition, it can identify the material types through normal pressing (based on the contact electrification) and identify the texture via relative sliding motion (based on the stick-slip phenomenon), respectively. Importantly, external pressure and contact materials are detected separately through independent sensory pathways. As a result, the BHES can be used to not only determine the types of contact materials but also precisely detect the pressure stimuli.

Single-electrode mode TENG and freestanding triboelectric-layer mode TENG are used for material type and texture recognition, respectively. The detailed design principle of deep learning enabled material and texture recognition modules is illustrated in Figure 1b. The material species can be determined when the BHES is pressed to contact the material, according to the output peak voltage produced due to the electron affinity differences of distinct materials. When the BHES is sliding across the surface of an object, the generated various output waveforms reflect the different texture/roughness of the object due to the fluctuated force and velocity generated through the stick-slip mechanism. Because the

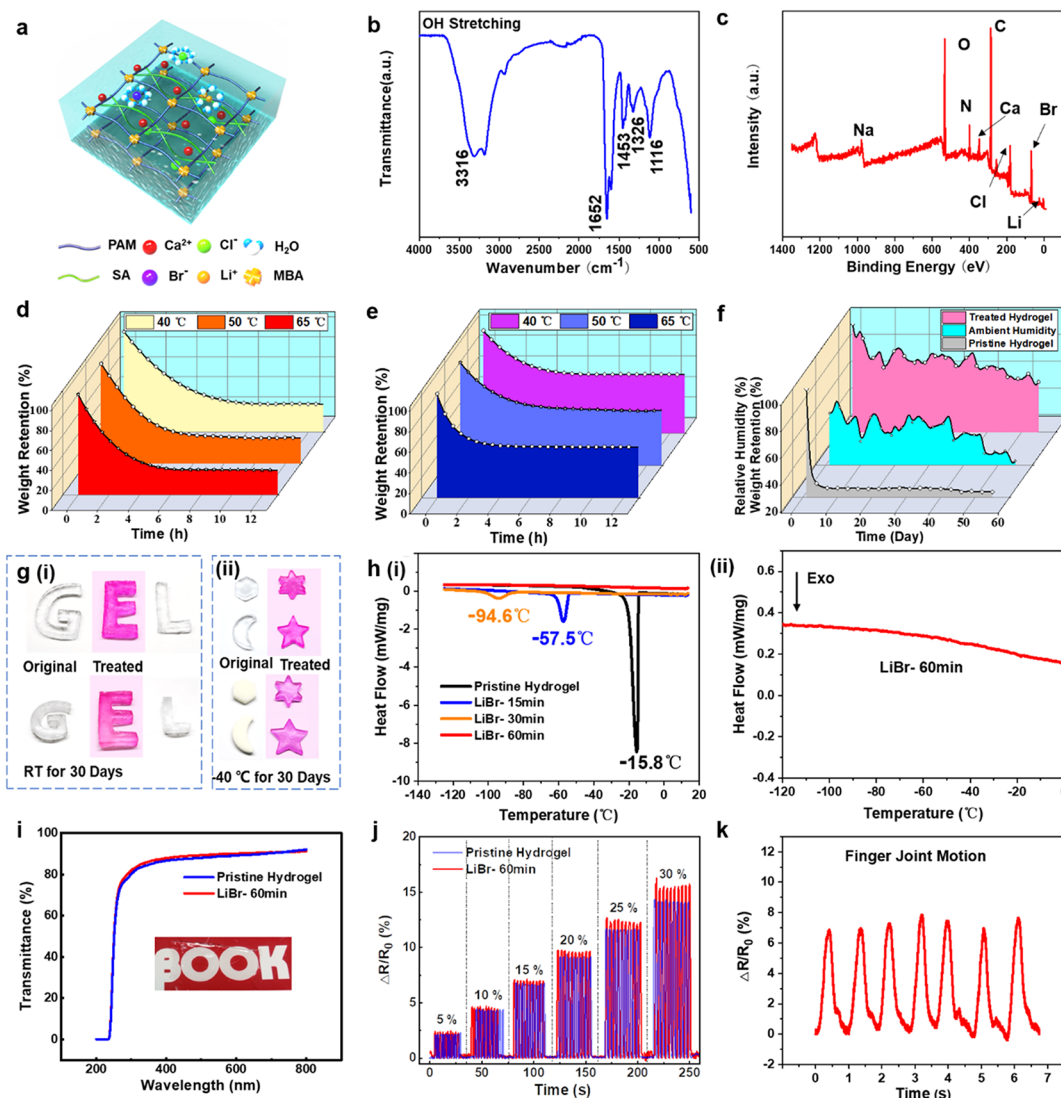


Figure 2. Characterization of various excellent properties of hydrogels. (a) The schematic illustration depicts the molecular architecture of LiBr immersion-treated PAM/CA DN hydrogel. (b) FTIR spectrum of the pristine DN hydrogel. (c) XPS spectrum of treated DN hydrogel. (d) Comparison of weight retention of the pristine hydrogel under 40, 50, and 65 °C at 30% RH. (e) Comparison of the anti-dehydrating characteristics of treated hydrogel under 40, 50, and 65 °C at 30% RH. (f) Weight retention of pristine hydrogel and treated hydrogel after being stored at RT for 60 days and the fluctuation of ambient relative humidity during this period. (g) i: Anti-dehydrating properties of the pristine hydrogel (G-shaped and L-shaped patterned hydrogel) and the treated hydrogel (E-shaped hydrogel marked in the pink region) stored at RT for 30 days; ii: Antifreezing characteristics of the pristine hydrogel and the treated hydrogel (marked in the pink region) in different polygon shapes stored at -40 °C for 30 days. (h) DSC measurement results of the pristine hydrogel and LiBr-treated hydrogel with different soaking time. (i) The transmittance spectra of pristine DN hydrogel and treated hydrogel. (j) Relative change in resistance at different strains of the pristine hydrogel and treated hydrogel. (k) Resistance variation curve of hydrogel when detecting finger motion.

minute differences in the generated signals may not be easily identified by human vision, artificial intelligence (AI) was used to distinguish the subtle differences of substances. Additionally, the BHES can achieve real-time gesture detection and convenient UAV control operation by adding a signal processing circuit, which has enormous application prospects in wearable electronics and interactive human-machine interfaces. With the assistance of AI, the BHES could endow the robot hand with the ability of both pressure detection and material/texture recognition, which can be developed for successful application of soft robotics in digital twin and metaverse applications of the BHES.

Micro/nano structures can significantly affect the properties of material and the device;^{63,64} for example, the micro-

structures on TENGs can significantly increase the contact areas during the triboelectrification process and thus improve the output performance of the devices.⁶⁵ Researchers have proposed a stretchable multimodal e-skin based on a wrinkle-patterned silicon elastomer, where the output signal under external mechanical stimuli was enhanced.^{66,67} In this article, the nanoscale wrinkle and microcone structures were introduced to the BHES. The microcone structures on the hydrogel surface with a bottom diameter of 250 μm and a height of 600 μm can be observed from the images by scanning electron microscopy (SEM), as shown in Figure 1c. Under pressure during pressing, the soft microcone structure is bent but not broken (Figure 1d). Ion beam etching (IBE) treatment was applied on the PET surface to generate and mimic the

wrinkled surface of the epidermal layer, enabling accurate identification of materials through the capabilities to gain/lose electrons during contact electrification. **Figure 1e** demonstrates the formed nanoscale wrinkle structure on the surface of PET after the IBE process. The SEM image in **Figure 1f** shows the multilayered structure of the compact device.

2.2. Characterization of Hydrogel with Multiple Prominent Properties. The transparent polyacrylamide (PAM)/calcium alginate (CA) DN hydrogel was synthesized using a simple polymerization process, as illustrated in **Figure S1**, Supporting Information and Experiment Section. Post-treatment for DN hydrogels was carried out by immersing the pristine DN hydrogel in a 50 wt % lithium bromide (LiBr) solution to introduce the hygroscopic LiBr, imparting it with antidehydrating and antifreezing capabilities. The molecular structure of LiBr solution-treated hydrogel is shown in **Figure 2a**, in which LiBr is ionized into Li^+ and Br^- in water, and they are bonded with the water molecules. A higher degree of ion hydration ensures a stronger bonding strength together with more bonded water molecules.

Figure 2b shows the Fourier transform infrared (FTIR) spectrum of the pristine DN hydrogel. The asymmetric C—O—C stretching and C—H deformation with the secondary alcohols are reflected by the peaks at 1116 and 1326 cm^{-1} , respectively, which are consistent with the molecular structure of alginate. Furthermore, the in-plane CH_2 scissoring and N—H stretching modes are identified from the peaks at 1453 and 3316 cm^{-1} , respectively, corresponding to the molecular structure of PAM. Hence, the FTIR results confirm the presence of PAM and CA double networks in the as-prepared hydrogels. Additionally, there is a wide and strong peak in the high wavenumber region (about 3400 cm^{-1}), revealing that there are plenty of hydrogen bonds inside the hydrogel. X-ray photoelectron spectroscopy (XPS) results shown in **Figure 2c** illustrate the elementary composition of the treated DN hydrogel, which reflects a generous amount of C (52.2%), medium content of O (17.01%), and tiny content of N (8.89%). Significantly, the strong ionic hydration effects are clearly verified by the detected Li (12.12%) and Br (5.79%) in the XPS spectrum of the treated hydrogel. Additionally, a tiny amount of Cl and Ca were also detected.

To compare the anti-dehydration capacities of the treated DN hydrogel and pristine DN hydrogel, both of them were placed in a chamber with 30% relative humidity (RH) for 12 h at different temperatures of 40, 50, and 65 °C, respectively, and the weight evolutions were recorded. Due to the inevitable water evaporation, the weights of both kinds of DN hydrogels are reduced. The treated DN hydrogel maintains higher residual masses, depicting its better anti-dehydration property than the untreated pristine hydrogel (as illustrated in **Figure 2d,e**). The weight retention of the treated DN hydrogel reaches 66.7, 62.0, and 45.7 wt % after being stored at 40, 50, and 65 °C for 12 h, respectively, which is primarily attributed to the strong bonding strength of hydrated ions. Besides, the weight retention of the sandwiched hydrogel can reach 72.9 wt % after being stored at 65 °C for 12 h, as shown in **Figure S2**. A long-term anti-dehydration experiment was further carried out for these two samples, which were placed at room temperature (RT) for 60 days accompanied by the random fluctuations in RH. As exhibited in **Figure 2f**, the weight retention of the untreated pristine hydrogel was reduced dramatically in the first 5 days but then stabilized at 22.9 wt % of the initial mass afterward. Nevertheless, the residual mass of the LiBr-treated

DN hydrogel varied with the fluctuation of ambient humidity, and a high consistency and positive correlation between the residual mass of the treated hydrogel and ambient humidity can be observed clearly, as shown in **Figure S3**.

To visually compare the anti-dehydration properties of the pristine and treated hydrogels, hydrogels with the character shapes of G, E, and L were formulated initially (**Figure 2g(i)**), followed by the LiBr solution immersion treatment of only the E-shaped hydrogel for an hour (marked in the pink region in **Figure 2g(i)**). After that, all of these samples were stored in a clean room for 30 days (25 °C and 60% RH). Significant shrinkage of untreated G-shaped and L-shaped hydrogels was observed, whereas the size of LiBr solution treated E-shaped hydrogel was not apparently altered. Furthermore, the antifreezing properties of both kinds of hydrogels were characterized. Similarly, hydrogels in different polygon shapes were prepared first, and part of them were soaked in 50 wt % LiBr solution for an hour (the treated part is marked in the pink region in **Figure 2g(ii)**). Subsequently, they were stored at −40 °C for 30 days in a refrigerator. The untreated hydrogel was frozen immediately, whereas the treated hydrogel remained in its original state without showing a frozen phenomenon.

Results obtained from the differential scanning calorimetry (DSC) spectra reveal the freezing temperatures of the pristine hydrogel and treated hydrogel with various LiBr immersion time. As illustrated in **Figure 2h(i)**, there is a sharp exothermic peak in the spectrum at around −15.8 °C for the pristine hydrogel, corresponding to its freezing point. Contrarily, the treated DN hydrogel exhibited much lower freezing temperatures; i.e., its freezing points were decreased from −57.5 to −94.6 °C as its soaking time in the LiBr solution was extended from 15 to 30 min. Interestingly, no any significant peak was observed on the DSC curve of the hydrogel that was treated for 1 h (**Figure 2h(ii)**), implying that the treated DN hydrogel can withstand a temperature below −120 °C. The excellent freezing and drying resistance of hydrogel should be attributed to the strong hydration effect of LiBr, as the formed stable $\text{Li}^+ \text{--} \text{H}_2\text{O}$ and $\text{Br}^- \text{--} \text{H}_2\text{O}$ clusters inhibit the freezing and evaporation of water molecules.

Moreover, the fabricated hydrogel also shows a high transparency, which is very useful for wearable electronics with the requirements of aesthetics and visibility. **Figure 2i** shows that the transmittance of both kinds of hydrogels could achieve over 85% in the visible spectrum, and the inset image indicates its high transparency. Additionally, the mechanical stability of the hydrogels was studied by stretching them for ten cycles under different strains. Results shown in **Figure 2j** display no significant fluctuation in the maximum $\Delta R/R_0$ values for both hydrogels after ten cycles. Here R_0 stands for the initial resistance of the hydrogel, while ΔR denotes the resistance variation. Furthermore, the hydrogel could also be used as a finger motion detection sensor based on the geometrical deformation effect during stretching, as shown in **Figure 2k**. The hydrogel film was attached to the finger joint firmly, and the resistance of the hydrogel was changed accordingly as the finger joints were moved. Furthermore, the hydrogel could also detect other human motions such as bending of wrist and knee (**Figure S4**), indicating its great potentials in wearable electronics. Moreover, the durability and reliable performance of the hydrogel were also investigated for its long-term applications (**Figure S5**). The developed hydrogel shows stable output when it was pressed and released for over

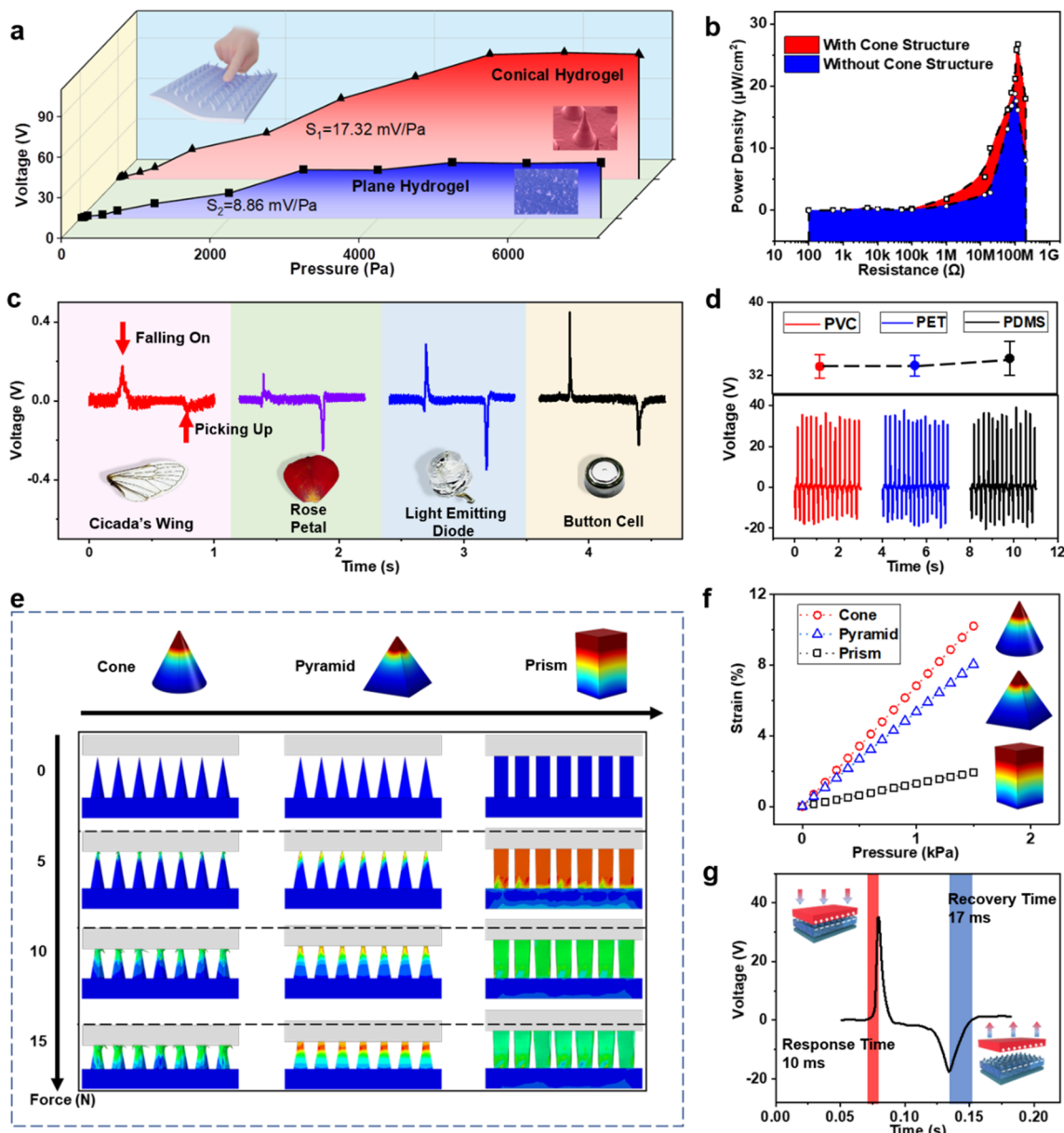


Figure 3. Characterization of pressure sensing module of the proposed BHES. (a) Comparison of sensitivities between sensors with micro conical hydrogel and plane hydrogel. (b) Dependence of the power density on the resistance of external load of the BHES with and without cone structures. (c) The output voltage of the BHES that was triggered by four ultralight objects. (d) Voltage curve when employing different materials to apply the same pressure to the BHES. (e) Finite element simulation of compression process of hydrogels with several microstructures: cone, pyramid, and prism. (f) Compressive strain under different pressures of three different microstructures. (g) The response and recovery time of the BHES.

1000 times, demonstrating its great potential for long-term applications.

2.3. Contact Materials-Unperturbed Pressure Sensing with High Sensitivity. As stated above, DN hydrogels have achieved many excellent properties. Accordingly, the micro-cone patterned hydrogel was used as both a conductive electrode and electrification layer of the BHES to constitute a self-powered pressure sensing module. The operating principle using this pressure sensing module of BHES is schematically shown in Figure S6. The output voltage of the proposed sensing device is created by the coupling of triboelectrification and electrostatic induction. When an external force is applied, the upper material recognition module layer was pressed down to the hydrogel layer, resulting in the formation of a contact

pair of PI and hydrogel. In this situation, the influence of the electron affinity of the contact material is reduced, thus achieving an accurate pressure sensing function, which was further verified by the experimental results. The output peak voltage is almost constant when poly(vinyl chloride) (PVC), PET, and PDMS exert the same pressure on the sensor (Figure 3d), demonstrating the sensor's excellent capacity to resist the interference of contacting materials. Since the electron affinities of PI and hydrogel are different, electrons will be transferred between contact surfaces. Then, the surfaces of these two materials carry equal charges with opposite polarity. When the external force is removed, the PI and hydrogel layers are separated, and the electrons will flow into the hydrogel layer through an external circuit until the electrostatic balance

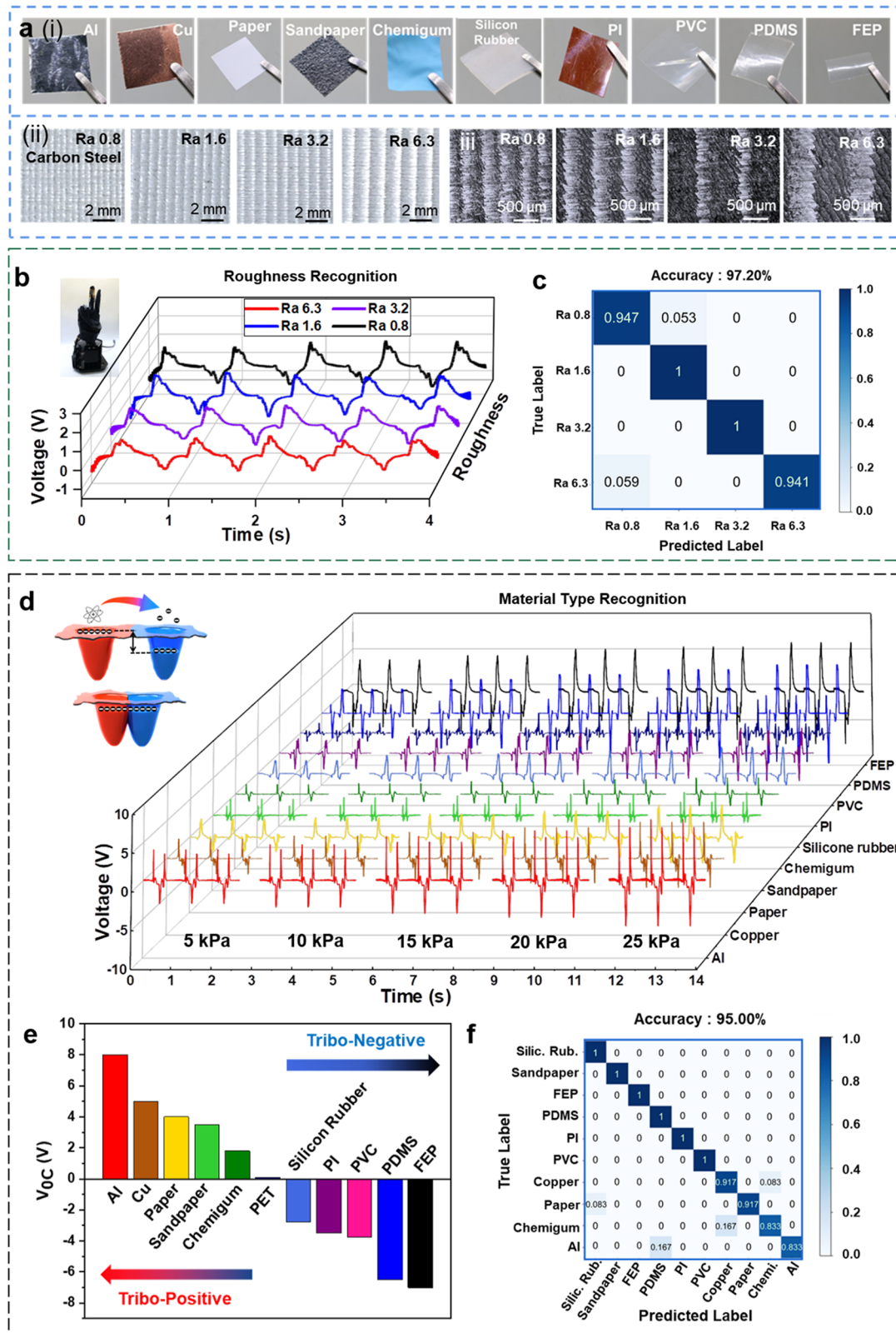


Figure 4. Material and roughness identification process and results. (a) i: The photographs of 10 materials; ii: Optical pictures of carbon steel with various roughness of Ra 0.8, Ra 1.6, Ra 3.2, and Ra 6.3 successively; iii: Optical microscope images of carbon steel with different roughness of Ra 0.8, Ra 1.6, Ra 3.2, and Ra 6.3 successively. (b) Obtained voltage signal waveforms when in contact with four carbon steel with different roughness, the inset image shows that the BHES is conformally attached to the robot hand. (c) The confusion matrix depicts the identification accuracy of different roughness. (d) The principle of electron transfer when various materials contact each other and the voltage signal acquired when the BHES press 10 kinds of materials under 5 various pressures. (e) V_{oc} of the BHES when it contacts 10 kinds of materials. (f) Confusion matrix result for the recognition of 10 materials.

is reached. Due to the resilience of the hydrogel, the higher contact pressure can cause the larger deformation of the hydrogel and provide larger contact area between PI and hydrogel to generate more triboelectric charges; thus, the output voltage is positively correlated with the applied pressure, which could be utilized to detect the pressure.

Different microstructures on the surface of the materials have considerable influences on their deformation behaviors, leading to different TENG responsiveness properties. In order to find the best deformable microstructure, deformation behaviors of three types of pressure sensors with different microstructures were simulated using finite element analysis (FEA), including BHESs with a microcone patterned hydrogel, a micropyramid patterned hydrogel, and a microprism patterned hydrogel. The deformability results of these three pressure sensors under compression are shown in Figure 3e. The strain is more uniformly distributed for the microprism patterned hydrogel, whereas it is more concentrated on the peak of the microcone patterned hydrogel than those of the microprism and micropyramid ones. The output voltage can be calculated using the equation as follows

$$V_{OC} = Q/C \quad (1)$$

where V_{OC} refers to the open-circuit voltage which is determined by the total triboelectric charge (Q) and the capacitance (C) of BHES. As the microcone patterned hydrogel is more easily deformed, a higher output voltage of TENG can be achieved due to the easily changeable capacitance (C). Figure 3f presents the simulation results of strain for three microstructures with comparable dimensions under various pressures. Obviously, the compressive strain of each microstructure demonstrates a positive correlation with the applied pressure. It is noteworthy that the strains of the microcone patterned hydrogel are significantly larger than those of the other two microstructured hydrogels under the same pressure within the investigated pressure range. In addition, the compression processes for these three microstructures were predicted theoretically, as illustrated in Note S1, Supporting Information. According to theoretical calculation results, the microcone patterned hydrogel exhibits a larger strain under the same stress than the other two kinds of micropatterned hydrogel of comparable sizes, which is consistent with simulation results.

Figure 3g displays the experimental dynamic response and recovery curve of BHES during pressing and releasing process under the pressure of around 2 kPa, demonstrating the fast response (10 ms) and recovery (17 ms) time, which are significantly faster than those of human skin (30–50 ms). To further examine the output performance of the BHES and illustrate the substantial effect of microcone structures, we created and analyzed both a plain BHES device and a microcone patterned device. The dependence of the output voltage on the pressure applied to these two devices is depicted in Figure 3a. During the test, a small vibration table was employed to exert force on the device. The excitation frequency was kept constant at 4 Hz. Clearly, the open-circuit voltages of both devices are increased initially with an increased external pressure. As the pressure increases, their output voltages gradually reach their maximum values. However, the microcone patterned BHES shows a much higher detection upper limit (5 kPa approximately) compared with that of plain BHES (3 kPa approximately). Importantly, the microcone patterned BHES reaches a sensitivity of 17.32

mV Pa⁻¹, which is almost twice as much as that of the unstructured BHES (i.e., 8.86 mV Pa⁻¹). This is mainly ascribed to the fact that the microcone patterned structure is easier to deform and effectively expands the contact area during the deformation process.

Additionally, the dependence of the power density on the external load resistance of the device with and without microcone structures was examined, as demonstrated in Figure 3b. The microcone patterned BHES has a much higher output voltage than those of the plain device within all measured external resistance range. Both of these devices attain their maximum power densities by using an approximately 100 MΩ resistance load. Furthermore, the microcone patterned BHES acquires a maximum peak power density of around 26.76 μW cm⁻², which is much higher than that of the plain device (18.78 μW cm⁻²). To intuitively demonstrate the sensitivity of the device to minor changes of pressure, the output voltages produced by four common ultralight objects (i.e., cicada's wing, rose petal, light-emitting diode, and a button cell) were generated, which are shown in Figure 3c. For example, the slight pressure of less than 20 Pa generated by falling of the cicada's wing can be perceived by the BHES. In addition, the stability and environmental compatibility of the BHES were also tested. As shown in Figure S7, the BHES could output stable voltage signals under the temperature of -27 and 65 °C. Besides, no significant decline on the maximum voltage was observed after 1000-time cyclic press-release test, which can contribute to its further long-term applications in different environments.

2.4. Pressure-Unperturbed Accurate Material and Texture Recognition. Identifying different types of materials is considered one of the crucial functions of human skin. Nevertheless, it is a huge challenge to use e-skins to achieve the correct identification of materials with identical smooth surfaces. Attributed to the creation of contact electrification and stick-slip mechanisms, the artificial e-skin in this study can exceed the ability of human skin and achieve precise material and texture recognition with the aid of deep learning techniques. The detailed operating principles of material and texture identification module of the BHES are schematically shown in Figure S8. In this study, 10 different materials including aluminum, copper, paper, sandpaper, Chemigum, silicone rubber, PI, PVC, and PDMS, alongside fluorinated ethylene propylene (FEP), and 4 milled carbon steel samples with different roughness values of Ra 0.8, Ra 1.6, Ra 3.2, and Ra 6.3 were chosen to verify the material species and surface roughness recognition capabilities of the BHES. Figure 4a exhibits the optical images of the above 10 materials and 4 different carbon steel samples. When another object slides on this rough surface, fluctuations in the friction and moving velocity can be generated. These irregular motions cause fluctuations in the sensing signals, which are applied as the principles for the identification of characteristics of the different textures. Inspired by the wrinkled surface of natural human skin, nanoscale wrinkled PET was introduced to constitute a friction pair with the touched objects and assist in texture identification through the stick-slip mechanism.

The obtained output signals of the BHES when attached to a robot hand and then slid on four carbon steel with various roughnesses are illustrated in Figure 4b, and the inset image shows the BHES which was conformally attached to the robot hand. Finally, the classification and identification of the signals were conducted with the aid of convolutional neural network

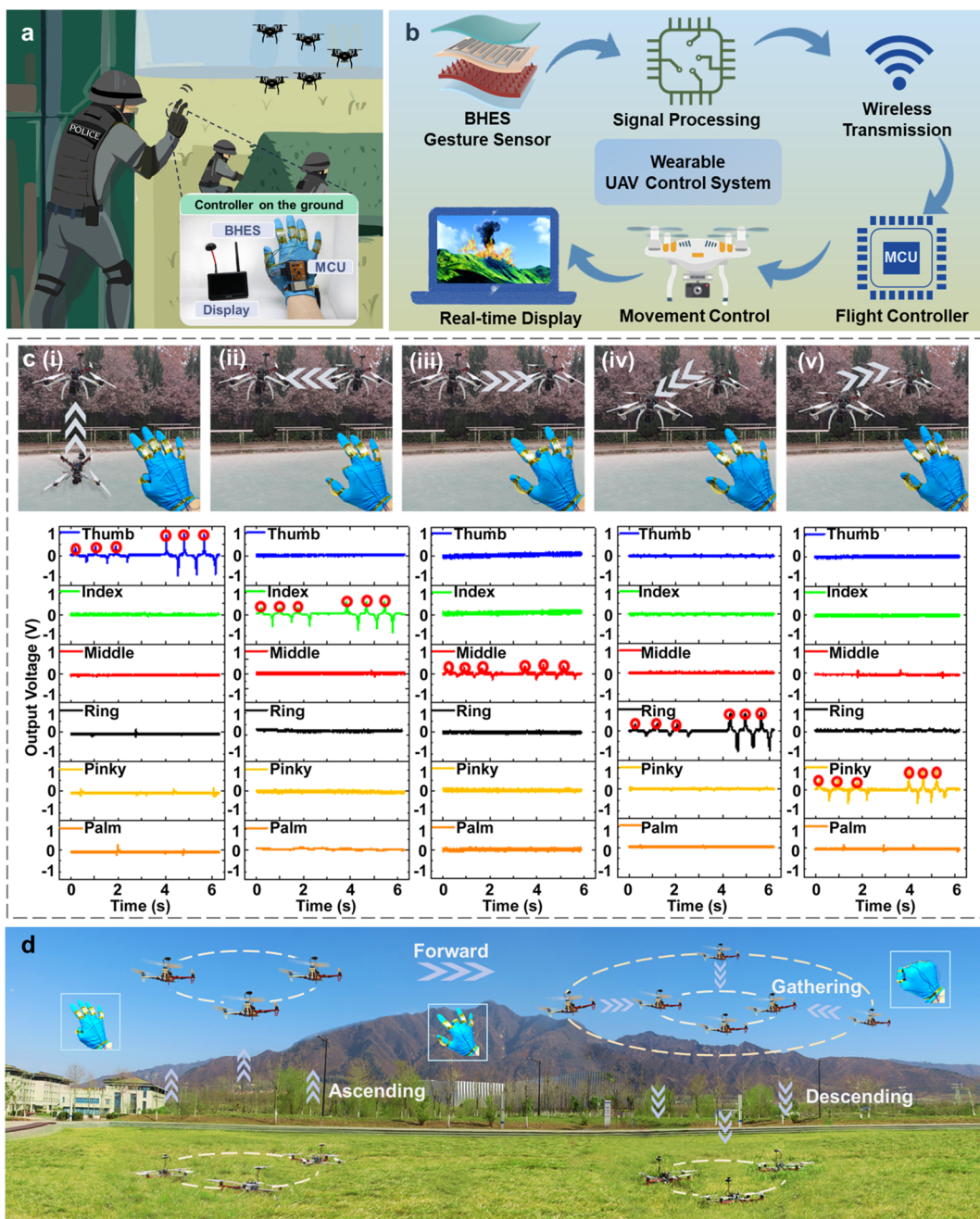


Figure 5. The implementation of the BHES for human–machine interfaces application. (a) Schematic representation of the proposed BHES-integrated UAV control system in a scenario of fighting against terrorism, and the inset image shows the setup of the BHES-integrated controller on the ground. (b) The schematic diagram depicts the working principle of the proposed drone control system. (c) Illustration and output signal of BHES attached to the hand when serving as 3-DOF UAV flight controller: (i) upward; (ii) left; (iii) right; (iv) forward; and (v) backward. (d) Illustration of the movement control of UAV swarms.

(CNN) because it can solve the problem that the slight distinction of the output signals could be hardly noticed by human vision and be easily ignored in manual features extraction, resulting in a poor recognition accuracy. The CNN can automatically extract valid features from the signals and give them higher weights to recognize. As for the data set, each category comprises 120 samples, where 96 samples were employed for training and 24 samples for testing, and the detailed information is shown in Note S2. After training the model iteratively, we acquired the confusion matrix of 4 kinds of roughness, as illustrated in Figure 4c, which has reached up to 97.20%.

Electron affinity is another significant characteristic of materials, which could aid in material recognition by generating different peak voltage for TENG. However, apart from the electron affinity, the contact pressure could also affect the output voltage. In this study, the BHES was applied with different pressures to press the 10 different types of materials with the help of a small vibration shaker. Figure 4d demonstrates the principle of electron transfer when different materials contact each other. It also shows the acquired voltage signal outputs when the BHES is pressed onto 10 kinds of materials under 5 different pressures. Clearly the output voltage is increased with the increased pressure when the

BHES presses a certain material. For practical applications, the contact pressure can be monitored by a pressure sensing module of the BHES, and thus the effect of the contact pressure can be minimized. Subsequently, the triboelectric series of these 10 materials compared with the PET surface is established, as illustrated in **Figure 4e**, which shows the relative electron affinity of the materials. The positive and negative voltage values exhibit the polarity of the charges after contact with the PET surface, while the magnitude of the voltage depicts the quantity of transferred charges; i.e., more transferred charges result in the higher output voltages. In this study, the average accuracy for material recognition can reach 95.00%, as illustrated in the confusion matrix in **Figure 4f**. Materials perceiving function of the BHES can contribute to bridge the physical and cyber word; thus, this work could be developed for the soft robots in digital twin and metaverse fields.

2.5. BHES-Integrated UAV Control System. Gestures are the highly efficient communication medium, especially for the antiterrorism scenario that needs soundless commutations. Accordingly, combining the human skin-inspired BHES with signal acquisition and wireless signal transmission circuit, a UAV control system is developed in this study, demonstrating its huge potentials in antiterrorism events, as illustrated in **Figure 5a**. The human hand motions are detected by the BHES, and the data are transferred to electrical output signals to manipulate the drones. The setup of the wearable drone control system is exhibited in **Figure 5a** and **Figure S9**.

Figure 5b illustrates a system-level overview of the drone control system, and the detailed control mechanism of manipulating drones by human hand gesture is demonstrated in **Figure S10**. The whole testing system contains three major components: 1) The flexible BHES sensors attached to the human fingers and palm are utilized to detect the movements of the finger joint and hand gestures. 2) Signal acquisition, processing, transmission circuit module, and driving control module are employed to collect and transmit the signals. 3) The controlled appliance (i.e., quadrotor) is manipulated. Once the BHES device generates the voltage signals, the outputs will be received by the microcontroller unit (MCU) on the ground directly. Subsequently, the MCU will process the voltage signals into six binary signals (0/1) under the predetermined threshold. These signals will be interpreted by an integrated flight controller module and then employed to drive electric motors, which will directly drive the drone in designable and controllable patterns.

The proposed BHES has been successfully utilized to regulate the quadrotor for human-machine interaction interface applications, as illustrated in **Figure 5c,d**. Five BHESs are attached on the second knuckles of each finger elaborately for the maximum moving range and hence the significant output signal of BHES. An extra one BHES is fastened closely on the palm, and all these six devices are designed for the three-degree-of-freedom (3-DoF) movement control of the drone. The BHES serves as the single-electrode TENG. Once the finger is bent, the BHES contacts the glove, and the output voltage impulse signals are obtained. The signals are then transmitted to the MCU in the air by a wireless transmission module. Subsequently, the drone receives instructions from the integrated flight controller and flies in the defined and controlled direction. Eventually, the 3-DoF flight of the quadrotor was regulated by the BHES successfully, as depicted in **Figure 5c**. The dynamic movements during the flights are

shown in **Movie S1**, Supporting Information. Besides, we have also demonstrated its applications for UAV swarms, which were manipulated by an elaborately designed control strategy, as demonstrated in **Figure 5d** and **Movie S2**.

In addition, the current developments of e-skins that could detect pressure, identify materials, or assist in drone control are summarized, as shown in **Table S2**. Through comparison, the proposed BHES demonstrates the outstanding properties with respect to functionalities and sensing performance. To be specific, a comprehensive study on e-skins like the BHES that could detect pressure, recognize the materials and textures with minimized interference, and control the UAV swarms is rarely reported. Besides, the BHES also shows advantages in fast and sensitive pressure sensing and accurate materials and textures recognition without external power source.

3. CONCLUSIONS

In this research, a human skin-inspired, ultrasensitive, and multifunctional hydrogel-based electronic skin was proposed by using nanoscale wrinkle patterned PET and microcone patterned DN hydrogel. The nanoscale wrinkle patterned PET was introduced in order to imitate the surface of the epidermis and generate the contact electrification mechanism. In addition, the microcone patterned DN hydrogel was employed as both the friction layer and conductive electrode to enhance the sensitivity of the device. The designed DN hydrogel shows superb anti-dehydration and antifreezing capacities, excellent transparency (over 85% in the visible spectrum), and admirable electrical stability. The elaborately designed BHES serves as the pressure sensor, which possesses a high sensitivity (17.32 mV/Pa) in a relatively wide pressure range (20–5000 Pa), a low detection limit, and ultrafast response (10 ms)/recovery (17 ms). The multifunctional BHES endows a robot with the capability of material identification and texture recognition. With the aid of deep learning, the recognition accuracy of 10 materials and 4 roughnesses are 95.00% and 97.20%, respectively. By further combining BHES with a signal acquisition/process circuit, the sensor shows its capacity as a human–machine interface to regulate UAV movements through monitoring human gestures. This research can be developed for intelligent robots in digital twin and metaverse applications and exhibits great potential in interactive human–machine interfaces.

4. EXPERIMENTAL SECTION

4.1. Preparation of Microcone Patterned PAM/CA DN Hydrogel. The 99% lithium bromide was purchased from Sigma–Aldrich. Dow Corning Inc. supplied poly(dimethylsiloxane) (PDMS Sylgard 184). The Ag wire with a diameter of 0.05 mm was provided by QingHe Silver Jewelry Corporation and was used as the conductive fabric. All the other chemicals, including acrylamide (AM), sodium alginate (SA), anhydrous calcium chloride, *N,N'*-methylenebis(acrylamide) (MBA), ammonium persulfate (AP), and *N,N,N',N'*-tetramethylethylenediamine were obtained from Aladdin. All of the reagents in this study were used as-received conditions without any refining, unless specially mentioned.

The PAM/CA DN hydrogel was synthesized via two steps, as depicted in **Figure S1**, Supporting Information. In the first step, 5.25 g of AM, 0.645 g of SA, 3 mg of MBA, and 30 mg of AP were dissolved in 30 mL of deionized (DI) water. A magnetic stirrer was utilized to stir the mixture at 750 rpm for 30 min. In this period, 10 μ L of *N,N,N',N'*-tetramethylethylenediamine was added as a cross-linking accelerator for the gelation process. Afterward, the produced solution was poured into a prefabricated PDMS mold, followed by vacuum treatment (-0.06 MPa for 5 min) to eliminate the inner air bubble.

Then, it was stored in an oven at a temperature of 65 °C for 2 h. Afterward, the produced hydrogel precursor was immersed into the 1 mol/L CaCl₂ solution at room temperature for 3 h. Sodium ions in SA were then replaced by calcium ions, creating the second ionically cross-linked CA network. Last but not least, the hydrogel was soaked in 50 wt % LiBr-saturated solutions for an hour to improve the antidrying and antifreezing performance.

4.2. Preparation of BHES. The nano- and micromachining processes were used to prepare the PDMS mold with microcone grooves. Using the PDMS mold, the above-mentioned facile polymerization method was used to create a microcone patterned hydrogel. The prepolymer and curing chemicals of PDMS were blended with a weight ratio of 10:1 and thoroughly stirred. Then, the precured solution was treated in a vacuum chamber (-0.06 MPa for 30 min) to eliminate the air bubble. To generate the PDMS substrate, the uncured PDMS precursor was spin-coated on an aluminum sheet at a rotation speed of 800 rpm for 30 s and dried in an oven at 70 °C for 2 h.

In the BHES material recognition module, the nanoscale wrinkle patterned PET was created after treatment with the IBE at an ion energy of 300 eV to create a feature and mimic the surface texture of human skin. Then, the commercial silver paste was sprayed to the back of the IBE-treated PET with the use of a 3D-printed mask with the interdigital pattern to fabricate the silver interdigital electrode with a 1-mm spacing and a thickness of 70 μm . Then, 30- μm -thick Kapton tape (3M Company) was pasted to the silver interdigital electrode and the PET. Finally, the material recognition module of the BHES was then glued to the PDMS substrate accompanied by the sandwiched hydrogels using double-sided sticky tape.

4.3. Material Characterization. Field-emission SEM (FESEM, VEGA 3 LMU) was utilized to characterize the morphology of the samples. The microcone patterned hydrogel without the LiBr solution treatment was coated with gold to obtain the SEM images for the sake of facile drying of the sample and, thus, easy vacuuming of the chamber. Additionally, the microcone patterned hydrogel was pressed when it was flexible, and during the pressing process, the hydrogel was dehydrated at RT. Ultimately, the SEM image of microcone patterned hydrogel under pressure was obtained. The FTIR result of the hydrogel was obtained using a Nicolet iS10 FTIR spectrometer. XPS spectrum of the LiBr-treated hydrogel was acquired using an XPS machine, Thermo Escalab 250Xi, Thermo Fisher Scientific Inc. The phase transition temperature of the pristine hydrogel and treated hydrogel was quantified using a DSC machine, DSC214 Polyma. The transmittance of the hydrogel was tested by employing a UV-vis spectrometer (Shimadzu UV-1780).

4.4. Electrical Output Characterization of Artificial Skin. The compression behaviors of the hydrogel with various microstructures were studied using the FEA software ABAQUS. The resistance variations of hydrogels with various tensile strain were measured on a tensile tester together with a digital multimeter (Keithley DMM6500). A vibration shaker was employed to generate periodic stimulations on the BHES. A commercial pressure sensor (FUTEK IPM650) was employed to estimate the external force of excitation. The open-circuit voltage of BHES was measured using a Keithley 6514 electrometer, and the high-impedance data acquisition system (NI USB-6289 DAQ Card) was also applied for multichannel voltage measurement.

ASSOCIATED CONTENT

Supporting Information

The Supporting Information is available free of charge at <https://pubs.acs.org/doi/10.1021/acsnano.3c05253>.

Notes, figures, and tables, mainly including theoretical calculated results about the deformability of three different structures; construction of neural network; diagram of preparing process of hydrogel; weight retention of the BHES under high temperature; dependence of the treated hydrogel's weight retention

on relative humidity; applications of DN hydrogel on human motion detection; stability of the hydrogel and BHES; operating principle of the pressure sensing module of BHES; operating principle of the material and texture identification module of BHES; setup of the controlled quadrotor in the air; principle of the proposed drone control system; sectional dimensions of cone and pyramid units; structure diagram of 1D-CNN for identification; the similarity between human skin and proposed highly biomimetic e-skin, and comparisons of the current e-skins ([PDF](#))

3-DoF unmanned aerial vehicle (UAV) control with six BHESs ([MP4](#))

UAV swarms control with the BHES-integrated control system ([MP4](#))

AUTHOR INFORMATION

Corresponding Authors

Jin Wu — State Key Laboratory of Optoelectronic Materials and Technologies and the Guangdong Province Key Laboratory of Display Material and Technology, School of Electronics and Information Technology, Sun Yat-sen University, Guangzhou 510275, China; Guangdong Provincial Key Laboratory of Technique and Equipment for Macromolecular Advanced Manufacturing, South China University of Technology, Guangzhou 510641, China;  orcid.org/0000-0002-3065-6858; Email: wujin8@mail.sysu.edu.cn

Haixia Zhang — National Key Laboratory of Science and Technology on Micro/Nano Fabrication; Beijing Advanced Innovation Center for Integrated Circuits, School of Integrated Circuits, Peking University, Beijing 100871, China; Email: zhang-alice@pku.edu.cn

Weizheng Yuan — Ministry of Education Key Laboratory of Micro and Nano Systems for Aerospace, School of Mechanical Engineering, Northwestern Polytechnical University, Xi'an 710072, China;  orcid.org/0000-0001-9490-7188; Email: yuanwz@nwpu.edu.cn

Authors

Kai Tao — Ministry of Education Key Laboratory of Micro and Nano Systems for Aerospace, School of Mechanical Engineering, Northwestern Polytechnical University, Xi'an 710072, China; Research & Development Institute of Northwestern Polytechnical University in Shenzhen, Sanhang Science & Technology Building, Shenzhen City 518063, China;  orcid.org/0000-0003-1848-8561

Jiahao Yu — Ministry of Education Key Laboratory of Micro and Nano Systems for Aerospace, School of Mechanical Engineering, Northwestern Polytechnical University, Xi'an 710072, China; Research & Development Institute of Northwestern Polytechnical University in Shenzhen, Sanhang Science & Technology Building, Shenzhen City 518063, China;  orcid.org/0009-0000-5980-1986

Jiyuan Zhang — Ministry of Education Key Laboratory of Micro and Nano Systems for Aerospace, School of Mechanical Engineering, Northwestern Polytechnical University, Xi'an 710072, China; Research & Development Institute of Northwestern Polytechnical University in Shenzhen, Sanhang Science & Technology Building, Shenzhen City 518063, China

Aocheng Bao — Ministry of Education Key Laboratory of Micro and Nano Systems for Aerospace, School of Mechanical

Engineering, Northwestern Polytechnical University, Xi'an 710072, China

Haowen Hu – Ministry of Education Key Laboratory of Micro and Nano Systems for Aerospace, School of Mechanical Engineering, Northwestern Polytechnical University, Xi'an 710072, China

Tao Ye – Ministry of Education Key Laboratory of Micro and Nano Systems for Aerospace, School of Mechanical Engineering, Northwestern Polytechnical University, Xi'an 710072, China;  orcid.org/0000-0001-9381-8781

Qiongling Ding – State Key Laboratory of Optoelectronic Materials and Technologies and the Guangdong Province Key Laboratory of Display Material and Technology, School of Electronics and Information Technology, Sun Yat-sen University, Guangzhou 510275, China

Yaozheng Wang – National Key Laboratory of Science and Technology on Micro/Nano Fabrication; Beijing Advanced Innovation Center for Integrated Circuits, School of Integrated Circuits, Peking University, Beijing 100871, China

Haobin Lin – State Key Laboratory of Optoelectronic Materials and Technologies and the Guangdong Province Key Laboratory of Display Material and Technology, School of Electronics and Information Technology, Sun Yat-sen University, Guangzhou 510275, China

Honglong Chang – Ministry of Education Key Laboratory of Micro and Nano Systems for Aerospace, School of Mechanical Engineering, Northwestern Polytechnical University, Xi'an 710072, China;  orcid.org/0000-0003-0400-3658

Complete contact information is available at:

<https://pubs.acs.org/10.1021/acsnano.3c05253>

Author Contributions

The manuscript was written through contributions of all authors. All authors have given approval to the final version of the manuscript.

Notes

The authors declare no competing financial interest.

ACKNOWLEDGMENTS

The authors thank Xinyue Du, Jinlin Wan, Shize Zhao, Jiacheng Zhang, and Xiaofan Du of Northwestern Polytechnical University for their experimental support. This research is supported by Shenzhen Science and Technology Program (JCYJ20220530161809020 & JCYJ20220818100415033), National Natural Science Foundation of China Grant (No. 52205137), the Fundamental Research Funds for the Central Universities, Sun Yatsen University (No. 22lgqb17).

REFERENCES

- (1) Someya, T.; Bao, Z. N.; Malliaras, G. G. The rise of plastic bioelectronics. *Nature* **2016**, *540*, 379–385.
- (2) Song, E.; Li, J.; Won, S. M.; Bai, W.; Rogers, J. A. Materials for flexible bioelectronic systems as chronic neural interfaces. *Nat. Mater.* **2020**, *19*, 590–603.
- (3) Li, G.; Liu, S.; Wang, L.; Zhu, R. Skin-inspired quadruple tactile sensors integrated on a robot hand enable object recognition. *Sci. Robot.* **2020**, *5*, No. eabc8134.
- (4) Han, M.; Wang, H.; Yang, Y.; Liang, C.; Bai, W.; Yan, Z.; Li, H.; Xue, Y.; Wang, X.; Akar, B.; Zhao, H.; Luan, H.; Lim, J.; Kandela, I.; Ameer, G. A.; Zhang, Y.; Huang, Y.; Rogers, J. A. Three-dimensional piezoelectric polymer microsystems for vibrational energy harvesting, robotic interfaces and biomedical implants. *Nat. Electron.* **2019**, *2*, 26–35.
- (5) He, J.; Xiao, P.; Lu, W.; Shi, J. W.; Zhang, L.; Liang, Y.; Pan, C. F.; Kuo, S. W.; Chen, T. A Universal high accuracy wearable pulse monitoring system via high sensitivity and large linearity graphene pressure sensor. *Nano Energy* **2019**, *59*, 422–433.
- (6) Cao, K. L.; Wu, M.; Bai, J. B.; Wen, Z.; Zhang, J. W.; Wang, T. Y.; Peng, M. W.; Liu, T.; Jia, Z.; Liang, Z. Q.; Jiang, L. Beyond Skin pressure sensing: 3D printed laminated graphene pressure sensing material combines extremely low detection limits with wide detection range. *Adv. Funct. Mater.* **2022**, *32*, 2202360.
- (7) Lee, S.; Byun, S. H.; Kim, C. Y.; Cho, S.; Park, S.; Sim, J. Y.; Jeong, J. W. Beyond human touch perception: an adaptive robotic skin based on gallium microgranules for pressure sensory augmentation. *Adv. Mater.* **2022**, *34*, No. 2204805.
- (8) Kwon, D.; Lee, T. I.; Shim, J.; Ryu, S.; Kim, M. S.; Kim, S.; Kim, T. S.; Park, I. Highly sensitive, flexible, and wearable pressure sensor based on a giant piezocapacitive effect of three-dimensional microporous elastomeric dielectric layer. *ACS Appl. Mater. Interfaces* **2016**, *8*, 16922–16931.
- (9) Lin, W.; Wang, B.; Peng, G.; Shan, Y.; Hu, H.; Yang, Z. Skin-inspired piezoelectric tactile sensor array with crosstalk-free row plus column electrodes for spatiotemporally distinguishing diverse stimuli. *Adv. Sci.* **2021**, *8*, 2002817.
- (10) Yuan, H.; Lei, T.; Qin, Y.; Yang, R. Flexible electronic skins based on piezoelectric nanogenerators and piezotronics. *Nano Energy* **2019**, *59*, 84–90.
- (11) Tao, K.; Chen, Z.; Yu, J.; Zeng, H.; Wu, J.; Wu, Z.; Jia, Q.; Li, P.; Fu, Y.; Chang, H.; Yuan, W. Ultra-sensitive, deformable, and transparent triboelectric tactile sensor based on micro-pyramid patterned ionic hydrogel for interactive human-machine interfaces. *Adv. Sci.* **2022**, *9*, No. 2104168.
- (12) Hu, Y.; Zhang, M.; Qin, C. R.; Qian, X. Y.; Zhang, L. N.; Zhou, J. P.; Lu, A. Transparent, conductive cellulose hydrogel for flexible sensor and triboelectric nanogenerator at subzero temperature. *Carbohydr. Polym.* **2021**, *265*, 118078.
- (13) Dai, C.; Ye, C.; Ren, J.; Yang, S.; Cao, L.; Yu, H.; Liu, S.; Shao, Z.; Li, J.; Chen, W.; Ling, S. Humanoid ionotronic skin for smart object recognition and sorting. *ACS Mater. Lett.* **2023**, *5*, 189–201.
- (14) Jin, T.; Sun, Z.; Li, L.; Zhang, Q.; Zhu, M.; Zhang, Z.; Yuan, G.; Chen, T.; Tian, Y.; Hou, X.; Lee, C. Triboelectric nanogenerator sensors for soft robotics aiming at digital twin applications. *Nat. Commun.* **2020**, *11*, 5381.
- (15) Qu, X.; Liu, Z.; Tan, P.; Wang, C.; Liu, Y.; Feng, H.; Luo, D.; Li, Z.; Wang, Z. L. Artificial tactile perception smart finger for material identification based on triboelectric sensing. *Sci. Adv.* **2022**, *8*, No. eabq2521.
- (16) Tee, B. C. K.; Chortos, A.; Berndt, A.; Nguyen, A. K.; Tom, A.; McGuire, A.; Lin, Z. L. C.; Tien, K.; Bae, W. G.; Wang, H. L.; Mei, P.; Chou, H. H.; Cui, B. X.; Deisseroth, K.; Ng, T. N.; Bao, Z. N. A skin-inspired organic digital mechanoreceptor. *Science* **2015**, *350*, 313–316.
- (17) Kim, Y.; Suh, J. M.; Shin, J.; Liu, Y.; Yeon, H.; Qiao, K.; Kum, H. S.; Kim, C.; Lee, H. E.; Choi, C.; Kim, H.; Lee, D.; Lee, J.; Kang, J.-H.; Park, B.-I.; Kang, S.; Kim, J.; Kim, S.; Perozek, J. A.; Wang, K.; et al. Chip-less wireless electronic skins by remote epitaxial freestanding compound semiconductors. *Science* **2022**, *377*, 859–869.
- (18) Cao, W.; Wang, Z.; Liu, X.; Zhou, Z.; Zhang, Y.; He, S.; Cui, D.; Chen, F. Bioinspired MXene-based user-interactive electronic skin for digital and visual dual-channel sensing. *Nano-Micro Lett.* **2022**, *14*, 119.
- (19) Chen, M.; Qian, X.; Cai, J.; Zhou, J.; Lu, A. Electronic skin based on cellulose/KCl/sorbitol organohydrogel. *Carbohydr. Polym.* **2022**, *292*, 119645.
- (20) Huang, H.; Feng, Y.; Yang, X.; Shen, Y. Natural gum-based electronic ink with water-proofing self-healing and easy-cleaning properties for directly on-skin electronics. *Biosens. Bioelectron.* **2022**, *214*, 114547.

- (21) Zhu, M.; Li, J.; Yu, J.; Li, Z.; Ding, B. Superstable and intrinsically self-healing fibrous membrane with bionic confined protective structure for breathable electronic skin. *Angew. Chem., Int. Ed.* **2022**, *61*, No. e202200226.
- (22) Zhang, J.; Hu, Y.; Zhang, L.; Zhou, J.; Lu, A. Transparent, ultra-stretching, tough, adhesive carboxyethyl chitin/polyacrylamide hydrogel toward high-performance soft electronics. *Nano-Micro Lett.* **2023**, *15*, 8.
- (23) Michalak, M.; Pierzak, M.; Krecisz, B.; Suliga, E. Bioactive compounds for skin health: a review. *Nutrients* **2021**, *13*, 203.
- (24) Nguyen, A. V.; Soulka, A. M. The dynamics of the skin's immune system. *Int. J. Mol. Sci.* **2019**, *20*, 1811.
- (25) Peng, X.; Dong, K.; Ye, C.; Jiang, Y.; Zhai, S.; Cheng, R.; Liu, D.; Gao, X.; Wang, J.; Wang, Z. L. A breathable, biodegradable, antibacterial, and self-powered electronic skin based on all-nanofiber triboelectric nanogenerators. *Sci. Adv.* **2020**, *6*, No. eaba9624.
- (26) Wang, H. L.; Guo, Z. H.; Pu, X.; Wang, Z. L. Ultralight iontronic triboelectric mechanoreceptor with high specific outputs for epidermal electronics. *Nano-Micro Lett.* **2022**, *14*, 86.
- (27) Kang, B. C.; Ha, T. J. Human-interactive drone system remotely controlled by printed strain/pressure sensors consisting of carbon-based nanocomposites. *Compos. Sci. Technol.* **2019**, *182*, 107784.
- (28) Kong, H.; Song, Z.; Li, W.; Bao, Y.; Qu, D.; Ma, Y.; Liu, Z.; Wang, W.; Wang, Z.; Han, D.; Niu, L. Skin-Inspired Hair-Epidermis-Dermis Hierarchical Structures for Electronic Skin Sensors with High Sensitivity over a Wide Linear Range. *ACS Nano* **2021**, *15*, 16218–16227.
- (29) Amoli, V.; Kim, J. S.; Jee, E.; Chung, Y. S.; Kim, S. Y.; Koo, J.; Choi, H.; Kim, Y.; Kim, D. H. A bioinspired hydrogen bond-triggered ultrasensitive ionic mechanoreceptor skin. *Nat. Commun.* **2019**, *10*, 4019.
- (30) Song, J. K.; Son, D.; Kim, J.; Yoo, Y. J.; Lee, G. J.; Wang, L.; Choi, M. K.; Yang, J.; Lee, M.; Do, K.; Koo, J. H.; Lu, N. S.; Kim, J. H.; Hyeon, T.; Song, Y. M.; Kim, D. H. Wearable Force Touch Sensor Array Using a Flexible and Transparent Electrode. *Adv. Funct. Mater.* **2017**, *27*, 1605286.
- (31) Wu, Z. X.; Wang, H.; Ding, Q. L.; Tao, K.; Shi, W. X.; Liu, C.; Chen, J.; Wu, J. A Self-Powered, Rechargeable, and Wearable Hydrogel Patch for Wireless Gas Detection with Extraordinary Performance. *Adv. Funct. Mater.* **2023**, *33*, 2300046.
- (32) Lu, B.; Yuk, H.; Lin, S.; Jian, N.; Qu, K.; Xu, J.; Zhao, X. Pure PEDOT:PSS hydrogels. *Nat. Commun.* **2019**, *10*, 1043.
- (33) Li, J.; Ding, Q.; Wang, H.; Wu, Z.; Gui, X.; Li, C.; Hu, N.; Tao, K.; Wu, J. Engineering Smart Composite Hydrogels for Wearable Disease Monitoring. *Nano-Micro Lett.* **2023**, *15*, 105.
- (34) Yuk, H.; Wu, J.; Zhao, X. Hydrogel interfaces for merging humans and machines. *Nat. Rev. Mater.* **2022**, *7*, 935–952.
- (35) Ding, Q.; Wang, H.; Zhou, Z.; Wu, Z.; Tao, K.; Gui, X.; Liu, C.; Shi, W.; Wu, J. Stretchable, self-healable, and breathable biomimetic iontronics with superior humidity-sensing performance for wireless respiration monitoring. *SmartMat* **2023**, *4*, No. e1147.
- (36) Liang, Y.; Wu, Z.; Wei, Y.; Ding, Q.; Zilberman, M.; Tao, K.; Xie, X.; Wu, J. Self-healing, self-adhesive and stable organohydrogel-based stretchable oxygen sensor with high performance at room temperature. *Nano-Micro Lett.* **2022**, *14*, 52.
- (37) Wei, H.; Lei, M.; Zhang, P.; Leng, J.; Zheng, Z.; Yu, Y. Orthogonal photochemistry-assisted printing of 3D tough and stretchable conductive hydrogels. *Nat. Commun.* **2021**, *12*, 2082.
- (38) Lim, C.; Hong, Y. J.; Jung, J.; Shin, Y.; Sunwoo, S. H.; Baik, S.; Park, O. K.; Choi, S. H.; Hyeon, T.; Kim, J. H.; Lee, S.; Kim, D. H. Tissue-like skin-device interface for wearable bioelectronics by using ultrasoft, mass-permeable, and low-impedance hydrogels. *Sci. Adv.* **2021**, *7*, No. eabd3716.
- (39) Zhai, K.; Wang, H.; Ding, Q.; Wu, Z.; Ding, M.; Tao, K.; Yang, B. R.; Xie, X.; Li, C.; Wu, J. High-performance strain sensors based on organohydrogel microsphere film for wearable human-computer interfacing. *Adv. Sci.* **2023**, *10*, No. 2205632.
- (40) Huang, S.; Hou, L.; Li, T.; Jiao, Y.; Wu, P. Antifreezing Hydrogel Electrolyte with Ternary Hydrogen Bonding for High-Performance Zinc-Ion Batteries. *Adv. Mater.* **2022**, *34*, 2110140.
- (41) Wang, C.; Liu, Y.; Qu, X.; Shi, B.; Zheng, Q.; Lin, X.; Chao, S.; Wang, C.; Zhou, J.; Sun, Y.; Mao, G.; Li, Z. Ultra-stretchable and fast self-healing ionic hydrogel in cryogenic environments for artificial nerve fiber. *Adv. Mater.* **2022**, *34*, 2105416.
- (42) Liu, X.; Inda, M. E.; Lai, Y.; Lu, T. K.; Zhao, X. Engineered living hydrogels. *Adv. Mater.* **2022**, *34*, 2201326.
- (43) Liu, Z.; Wang, Y.; Ren, Y.; Jin, G.; Zhang, C.; Chen, W.; Yan, F. Poly(ionic liquid) hydrogel-based anti-freezing ionic skin for a soft robotic gripper. *Mater. Horiz.* **2020**, *7*, 919–927.
- (44) Ding, Q. L.; Zhou, Z. J.; Wang, H.; Wu, Z. X.; Tao, K.; Yang, B. R.; Xie, X.; Fu, J.; Wu, J. Self-healable, recyclable, ultrastretchable, and high-performance NO₂ sensors based on an organohydrogel for room and sub-zero temperature and wireless operation. *SmartMat* **2023**, *4*, No. e1141.
- (45) Zhang, X.-F.; Ma, X.; Hou, T.; Guo, K.; Yin, J.; Wang, Z.; Shu, L.; He, M.; Yao, J. Inorganic salts induce thermally reversible and anti-freezing cellulose hydrogels. *Angew. Chem., Int. Ed.* **2019**, *58*, 7366–7370.
- (46) Zhu, T.; Jiang, C.; Wang, M. L.; Zhu, C. Z.; Zhao, N.; Xu, J. Skin-inspired double-hydrophobic-coating encapsulated hydrogels with enhanced water retention capacity. *Adv. Funct. Mater.* **2021**, *31*, 2102433.
- (47) Zhou, Z.; Qian, C.; Yuan, W. Self-healing, anti-freezing, adhesive and remoldable hydrogel sensor with ion-liquid metal dual conductivity for biomimetic skin. *Compos. Sci. Technol.* **2021**, *203*, 108608.
- (48) Wang, H.; Han, M.; Song, Y.; Zhang, H. Design, manufacturing and applications of wearable triboelectric nanogenerators. *Nano Energy* **2021**, *81*, 105627.
- (49) Li, Y.; Zhao, M.; Yan, Y.; He, L.; Wang, Y.; Xiong, Z.; Wang, S.; Bai, Y.; Sun, F.; Lu, Q.; Wang, Y.; Li, T.; Zhang, T. Multifunctional biomimetic tactile system via a stick-slip sensing strategy for human-machine interactions. *npj Flexible Electron.* **2022**, *6*, 46.
- (50) Song, Z. W.; Yin, J. H.; Wang, Z. H.; Lu, C. Y.; Yang, Z.; Zhao, Z. H.; Lin, Z. N.; Wang, J. Y.; Wu, C. S.; Cheng, J.; Dai, Y.; Zi, Y. L.; Huang, S. L.; Chen, X. L.; Song, J.; Li, G.; Ding, W. B. A flexible triboelectric tactile sensor for simultaneous material and texture recognition. *Nano Energy* **2022**, *93*, 106798.
- (51) Tao, K.; Yi, H. P.; Yang, Y.; Chang, H. L.; Wu, J.; Tang, L. H.; Yang, Z. S.; Wang, N.; Hu, L. X.; Fu, Y. Q.; Miao, J. M.; Yuan, W. Z. Origami-inspired electret-based triboelectric generator for biomechanical and ocean wave energy harvesting. *Nano Energy* **2020**, *67*, 104197.
- (52) Fan, F.-R.; Tian, Z.-Q.; Lin Wang, Z. Flexible triboelectric generator! *Nano Energy* **2012**, *1*, 328–334.
- (53) Pu, X.; Liu, M.; Chen, X.; Sun, J.; Du, C.; Zhang, Y.; Zhai, J.; Hu, W.; Wang, Z. L. Ultrastretchable, transparent triboelectric nanogenerator as electronic skin for biomechanical energy harvesting and tactile sensing. *Sci. Adv.* **2017**, *3*, No. e1700015.
- (54) Tao, K.; Chen, Z.; Yi, H.; Zhang, R.; Shen, Q.; Wu, J.; Tang, L.; Fan, K.; Fu, Y.; Miao, J.; Yuan, W. Hierarchical honeycomb-structured electret/triboelectric nanogenerator for biomechanical and morphing wing energy harvesting. *Nano-micro Lett.* **2021**, *13*, 123.
- (55) Ahmed, A.; Guan, Y.-S.; Hassan, I.; Ling, C.; Li, Z.; Mosa, I.; Phadke, G.; Selvaganapathy, P. R.; Chang, S.; Ren, S. Multifunctional smart electronic skin fabricated from two-dimensional like polymer film. *Nano Energy* **2020**, *75*, 105044.
- (56) Yuan, F.; Liu, S.; Zhou, J. Y.; Wang, S.; Wang, Y.; Xuan, S. H.; Gong, X. L. Smart touchless triboelectric nanogenerator towards safeguard and 3D morphological awareness. *Nano Energy* **2021**, *86*, 106071.
- (57) Lin, L.; Xie, Y. N.; Wang, S. H.; Wu, W. Z.; Niu, S. M.; Wen, X. N.; Wang, Z. L. Triboelectric Active Sensor Array for Self-Powered Static and Dynamic Pressure Detection and Tactile Imaging. *ACS Nano* **2013**, *7*, 8266–8274.

- (58) Fagiani, R.; Massi, F.; Chatelet, E.; Berthier, Y.; Akay, A. Tactile perception by friction induced vibrations. *Tribol. Int.* **2011**, *44*, 1100–1110.
- (59) Delhaye, B.; Hayward, V.; Lefevre, P.; Thonnard, J.-L. Texture-induced vibrations in the forearm during tactile exploration. *Front. Behav. Neurosci.* **2012**, *6*, 37.
- (60) Huang, S.; Misra, A. Micro-Macro-Shear-Displacement Behavior of Contacting Rough Solids. *Tribol. Lett.* **2013**, *51*, 431–436.
- (61) Niu, H.; Li, H.; Gao, S.; Li, Y.; Wei, X.; Chen, Y.; Yue, W.; Zhou, W.; Shen, G. Perception-to-cognition tactile sensing based on artificial-intelligence-motivated human full-skin bionic electronic skin. *Adv. Mater.* **2022**, *34*, No. 2202622.
- (62) Wei, X.; Li, H.; Yue, W.; Gao, S.; Chen, Z.; Li, Y.; Shen, G. A high-accuracy, real-time, intelligent material perception system with a machine-learning-motivated pressure-sensitive electronic skin. *Matter* **2022**, *5*, 1481.
- (63) Shin, H.; Kim, D.-H.; Jung, W.; Jang, J.-S.; Kim, Y. H.; Lee, Y.; Chang, K.; Lee, J.; Park, J.; Namkoong, K.; Kim, I.-D. Surface Activity-Tuned Metal Oxide Chemiresistor: Toward Direct and Quantitative Halitosis Diagnosis. *ACS Nano* **2021**, *15*, 14207–14217.
- (64) Yun, T. G.; Jang, J.-S.; Cheong, J. Y.; Kim, I.-D. Organism epidermis/plant-root inspired ultra-stable supercapacitor for large-scale wearable energy storage applications. *Nano Energy* **2021**, *82*, 105776.
- (65) Chen, Z.; Yu, J.; Zhang, X.; Zeng, H.; Li, Y.; Wu, J.; Tao, K. A button switch inspired duplex hydrogel sensor based on both triboelectric and piezoresistive effects for detecting dynamic and static pressure. *Nanotechnology and Precision Engineering* **2022**, *5*, 023002.
- (66) Lee, G.; Son, J. H.; Lee, S.; Kim, S. W.; Kim, D.; Nguyen, N. N.; Lee, S. G.; Cho, K. Fingerpad-Inspired Multimodal Electronic Skin for Material Discrimination and Texture Recognition. *Adv. Sci.* **2021**, *8*, 2002606.
- (67) Lee, G.; Zarei, M.; Wei, Q.; Zhu, Y.; Lee, S. G. Surface Wrinkling for Flexible and Stretchable Sensors. *Small* **2022**, *18*, 2203491.



CAS BIOFINDER DISCOVERY PLATFORM™

PRECISION DATA FOR FASTER DRUG DISCOVERY

CAS BioFinder helps you identify targets, biomarkers, and pathways

Unlock insights

CAS
A division of the
American Chemical Society